Supplement of Atmos. Chem. Phys., 21, 7293–7319, 2021
https://doi.org/10.5194/acp-21-7293-2021-supplement

Atmospheric Chemistry and Physics
Open Access

Supplement of

Measurement report: Fourteen months of real-time characterisation of the submicronic aerosol and its atmospheric dynamics at the Marseille–Longchamp supersite

Benjamin Chazeau et al.

Correspondence to: Benjamin Chazeau (benjamin.chazeau@univ-amu.fr) and Nicolas Marchand (nicolas.marchand@univ-amu.fr)

SUPPLEMENTARY FIGURES

Figure S1. The map on the left shows the location of the supersite MRS-LCP (white square). The grey arrow indicates the industrial area location and coloured dots correspond to ship positions from different basins in Marseille port: red dots are for south basin, green for east basin, and blue for north basin. In the lower left–hand corner the rose plot of wind speed and wind direction is represented for the full study period. Map provided by Google Earth Pro v7.3.3.7786, Data SIO, NOAA, U.S. Navy., NGA, GEBCO © 2020 Google.

Calibrations	RIE_{NH4}	RIE_{SO4}
05/19/2017	3.3	0.92-0.98
06/28/2018	2.4	0.8-0.9
12/07/2018	3	0.91

Table S1. RIEs determined during several calibrations at MRS-LCP supersite.

Ammonium	Nitrate	Organic	Sulfate	Chlore
0.098	0.018	0.55	0.034	0.021

Table S2. Detection limit in µg m^{-3} (3*σ) of chemical species from ToF-ACSM.

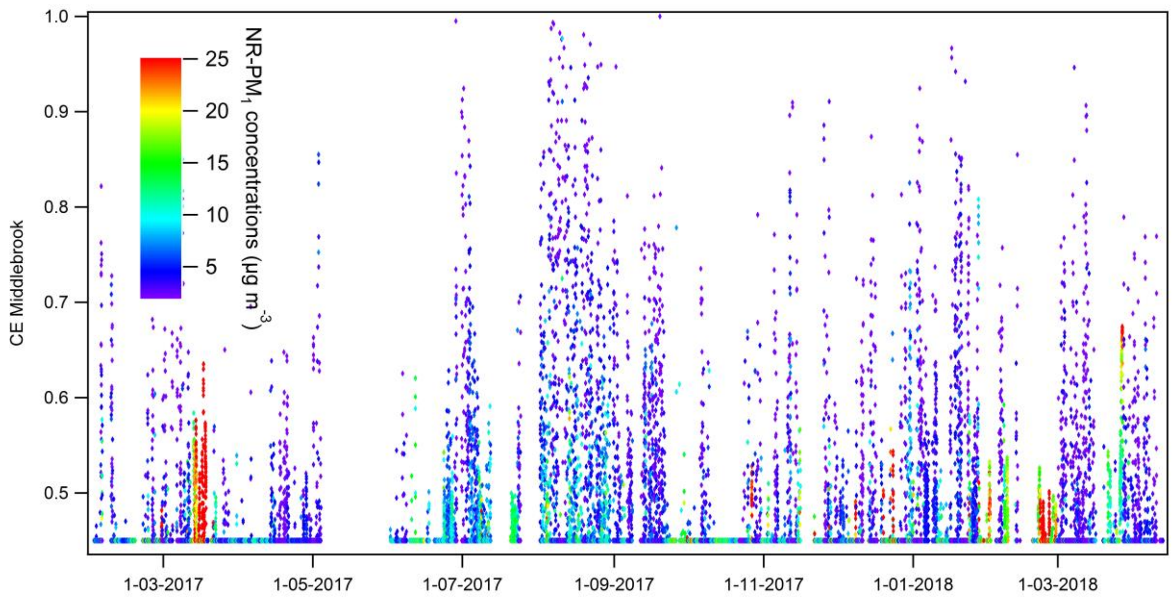

Figure S2. Temporal trend of collection efficiency (CE) from Middlebrook calculations colored according to the NR-PM$_1$ concentrations, for the full period of ACSM measurements.

Equation S1. Pieber correction: True_CO2+(t) = measured_CO2+(t) - b*NO(t)+ - b*NO2+(t)

Calibrations (mm/yy)	**b (Pieber effect)**	**NO2+/NO+**
12/16	0.0053	0.5631
05/17	0.0039	0.5604
06/18	0.0011	0.5730
12/18	0.0022	0.5604
Average	**0.0032**	**0.5642**
Standard errors	**0.0009**	**0.0244**

Table S3. Overview of b value used for Pieber correction and NO_2^+/NO^+ ratios measured during ToF-ACSM calibrations:

Equation S2. NO^+ = 30,-frag_air[30], frag_organic[30],-0.215*frag_organic[29]

NO_2^+ = 46,-0.127*45

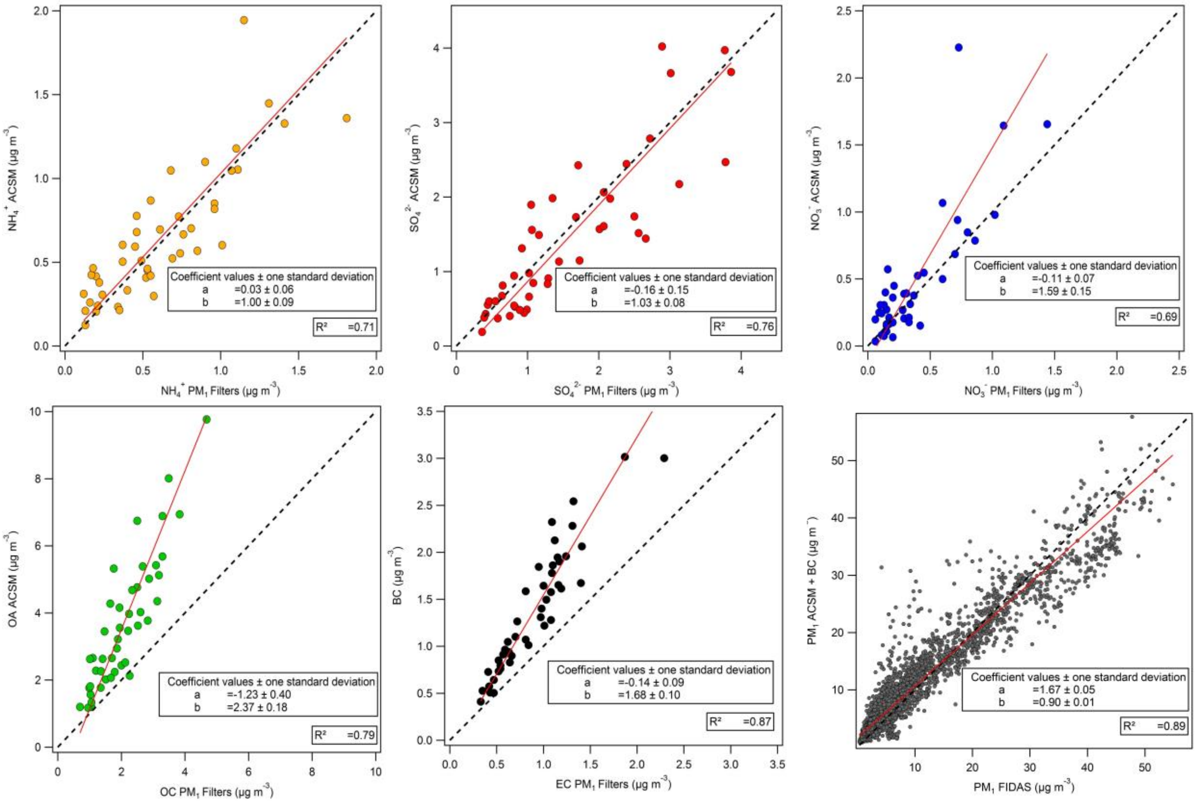

Figure S3. BC and ACSM species concentrations vs PM$_1$ 24h filters analysed respectively for EC, nitrate, OC (compared to organic matter from ACSM measurements), ammonium and sulfate. Reconstructed PM$_1$ (ACSM+BC) are also compared to PM$_1$ measurements from the FIDAS for a 3 months from February to April 2018. Red lines correspond to orthogonal distance fits between species and filters. R^2 are from least square fits.

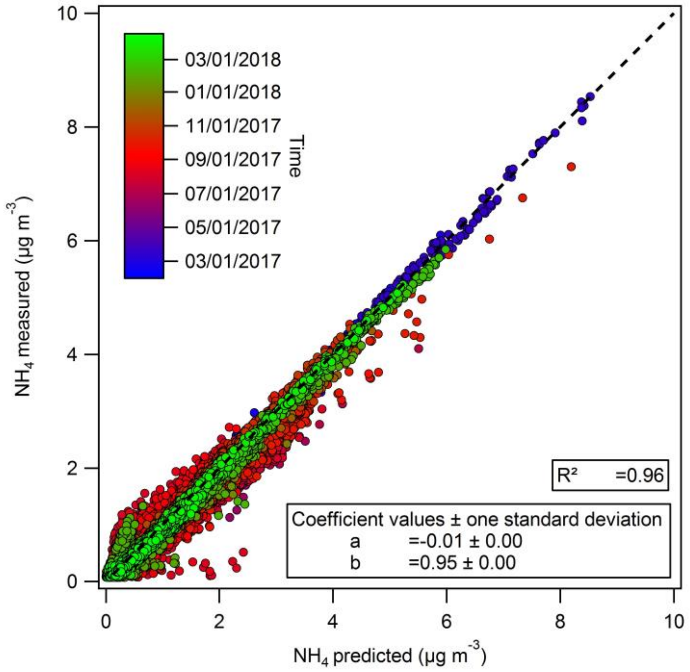

Figure S4. NH_4 measured (directly from TOF-ACSM) vs NH_4 predicted (calculated from Cl^-, NO_3^- and SO_4^{2-}) for ionic balance evaluation. Black dashed-line is the 1:1 line and the fit coefficients are from orthogonal distance fit.

The Angström exponent's determination:

As a first step the procedure recommended by Zotter et al. (2017) (i.e. to use the 470 and 950 nm wavelengths with an Angström exponent of 1.68 and 0.9 for pure wood burning and fossil fuel respectively) was applied. Using the suggested values led to unrealistic high BC_{WB} contributions in the summer (18%) when biomass burning is expected to be negligible during the hot period. It is hypothesised, as previously suggested by (Titos et al., 2017), that a fraction of BC_{FF} was wrongly attributed to wood burning as a consequence of a failure of the model to reconstruct sources when the biomass burning fraction is very low. This potential bias was investigated on fossil fuel-derived PM_1 from a urban traffic site (station "Kaddouz", location: 43°34'49.8" N;5°37'49.3" E) during summer time. This kerbside site is located at the portal of a tunnel in the surrounding area of Marseille. In order to inspect the different combinations of Angström exponent for fossil fuel and wood burning (α_{FF} and α_{WB}, respectively) a sensitivity test was performed by scanning combination changes in a α_{FF} range of 0.9-1.1 and a α_{WB} range 1.6-2 with a step size of 0.01. From this analysis a set of 861 combinations was evaluated and optimized based on the BC_{WB} diurnal cycles, which must significantly differ from BC_{FF} diurnal profiles. All the 861 diurnal cycles were categorized according to a k-means clustering analysis. This technique allowed to group the results into a specific number of clusters (Figure Sa) based on the protocols from Elser et al. (2016) and Bozzetti et al. (2017).

The analysis aims at classify a dataset into k clusters by minimizing the term T1 from the cost function (CF), which represents the sum of the Euclidian distances between each data point (x_i) and its respective cluster center μ_{zi} according to equation (S3). In order to select the right number of clusters the same strategy as Elser et al. (2016) and Bozzetti et al. (2017) is used. The goal is to explicitly penalize the addition of a new cluster by using the Bayesian information criteria, given as the product between the number of cluster k and the logarithm of the dimensionality of the clusters D (=24 here, which correspond to the number of hours from the diurnal cycles).

$$T1 = \sum_{i,z}\left((x_i - \mu_{z,i})^2\right) \ , \tag{S3}$$

$$CF = T1 + T2 = \sum_{i,z}\left((x_i - \mu_{z,i})^2\right) \ + k \ .\log(D) \ , \tag{S4}$$

At the end the cost function which has to be minimized is described in equation (S4). Figure S5a displays a minimum in the cost function at five clusters. Thus the 5 clusters solution was retained to describe the BC_{WB} diurnal variability according to the different set of Angsröm exponents.

The diurnal evolutions of BC_{WB} for different Angström exponent's α_{FF} and α_{WB} show a two-peak diurnal pattern typical of traffic similarly to BC_{FF} when considering the clusters 1, 2 and 4. For cluster 5 the diurnal cycle was negative suggesting wrong assignments of the model, while cluster 3 showed a smooth wood burning profile and reduced concentrations close to 0, which is expected for a kerbside site. The possible combinations of Angström exponents for this cluster are represented in Figure Sb (pink area).

To reduce the current multitude of possibilities a second criterion of selection is optimized, which is the minimum number of $BC_{WB}<0$ points (i.e. $BC_{FF}>BC$) as determined by Petit et al. (2017). Among the previous selection (cluster 3) this minimum number is inspected and found for an α_{FF} = 1.02 and an α_{WB} = {1.6; 2} (Figure Sc). An α_{FF} of 1.02 would be more representative of fresh traffic emission in Marseille and Garg et al. (2016) suggested that $\alpha_{FF} > 1$ could be more appropriate for older vehicles operating with poorly optimized engines.. As no more criterion allow to reduce α_{WB} , a reference value of 1.68 from Zotter et al. (2017) has been used for this study. Final diurnal evolutions for “Kaddouz” site are presented in Figure S5b.

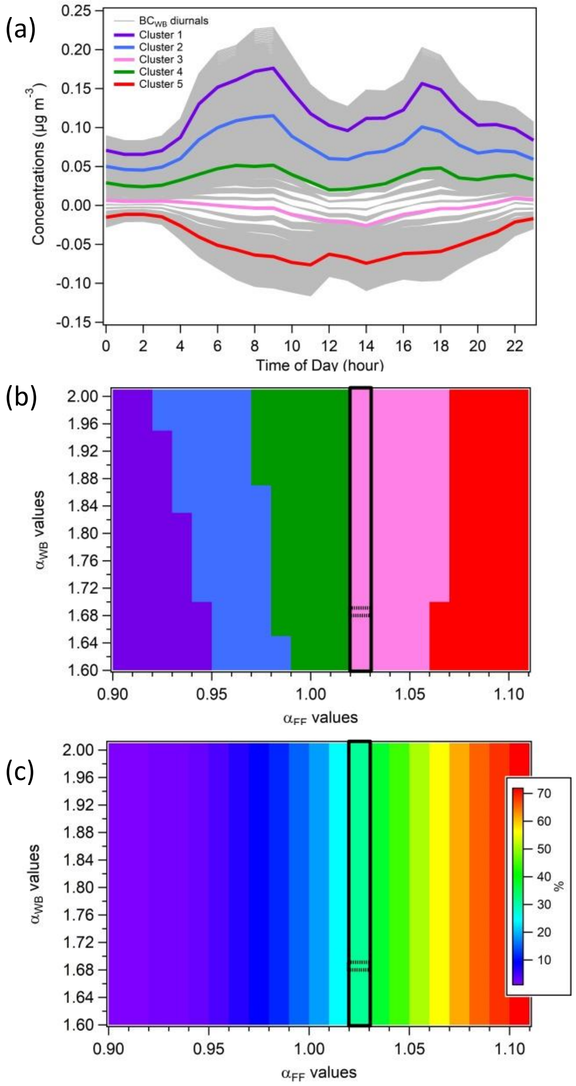

Figure S5. Cluster analysis of the BCWB diurnal cycles from "Kaddouz" station in summer 2017. Five clusters are presented according different colors (cluser 1 = violet; cluster 2 = blue; cluster 3 = pink; cluster 4 = green; cluster 5 = red). (a) represents all BC$_{WB}$ diurnals (in grey) from the sensitivity test and the colored cluster diurnals. (b) represents the cluster assignment for all Angström exponents combinations and (c) shows the number of BC$_{WB}$<0 points (in %) according to a rainbow color scale. For (b) and (c) the area surrounded with black line includes all accepted combinations, and the black dashed line correspond to the selected combination in this study (α_{FF}=1.02 and α_{WB}=1.68).

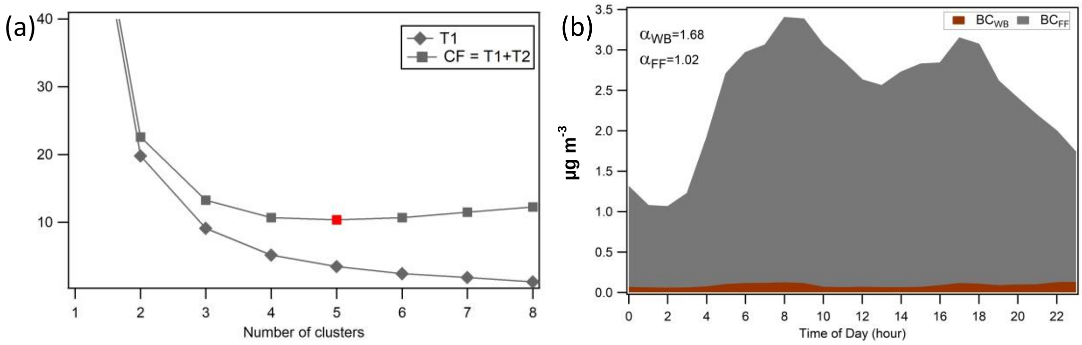

Figure S5. Number of cluster selection according to T1 (diamond markers) and the cost function (T1+T2) (square markers) (a). The red marker represents the minimum value and thus the number of cluster selected. For more clarity, data points are zoomed between 2 and 8 clusters. Diurnal evolutions of BC_{WB} and BC_{FF} recorded at kerbside "Kaddouz" site during summer 2017 (b). Sensitivity analyses were performed on α_{WB} and α_{FF} combinations in the aethalometer model to evaluate most realistic patterns for the two sources.

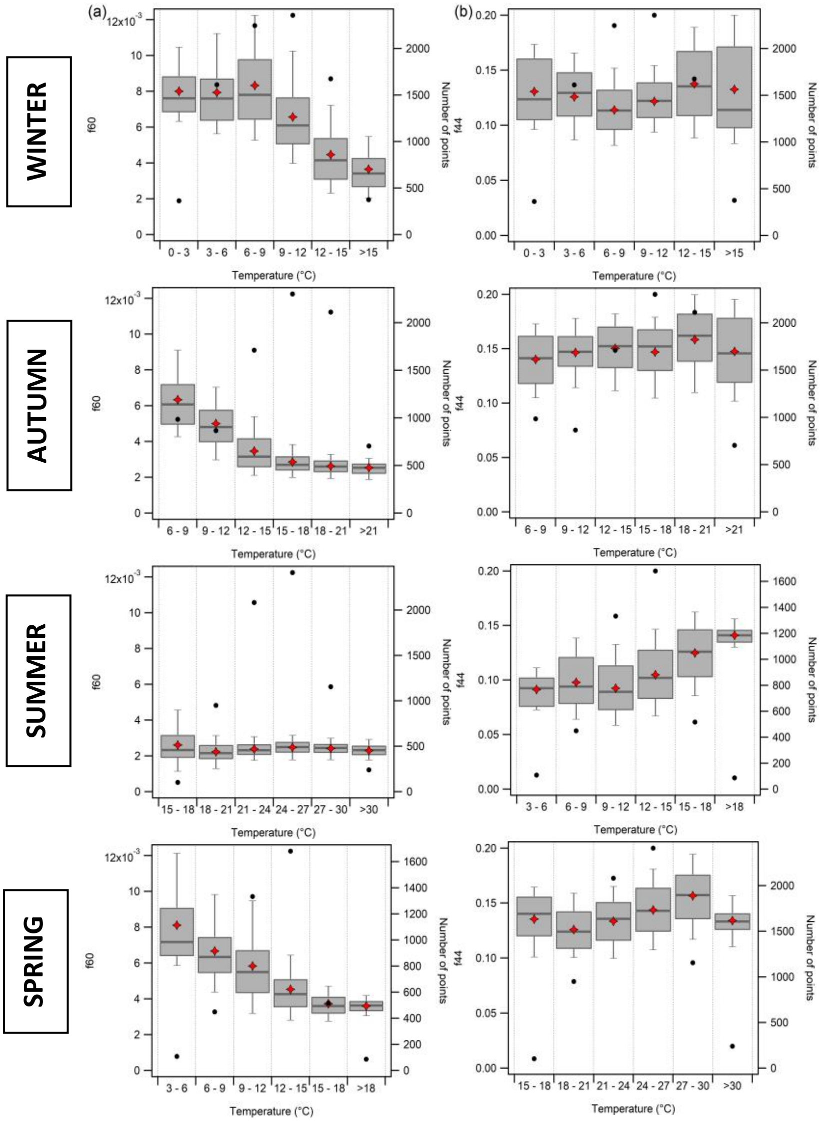

Figure S7. Seasonal box plots of f60and f44 as a function of ambient temperature bins. The red diamonds correspond to averages, the bands inside the box are the median, the bottom and top of the box represent the lower and upper quartiles respectively and the ends of the whiskers show the 10th and 90th percentile. The black circles show on the right axis the number of points encountered in each bin. Note the different scales of temperature bins according to seasons for a better visualization.

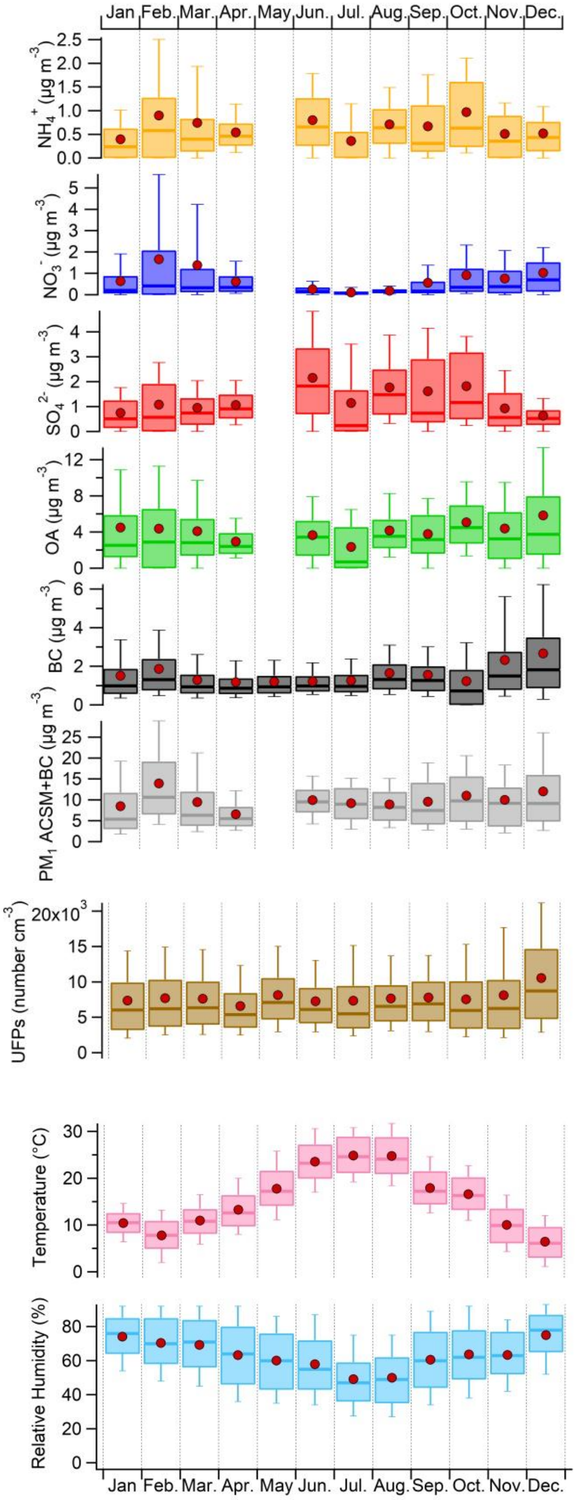

Figure S8. Monthly box plots of PM_1 chemical species, total PM_1 concentrations, UFPs (20-100nm) from 3031 monitor, temperature and relative humidity (from the Vaudran station). The band inside the box is the median (50th percentile), the bottom and top of the box represent the lower and upper quartiles respectively (the 25th and the 75th percentile). The ends of the whiskers denote here the 10th and 90th percentile. The red dots refer to the mean of each component.

Description of the organic nitrate calculation from ToF-ACSM measurements

Many past studies have demonstrated the possibility to separate the contribution of inorganic ($NO_{3,Inorg}$) and organic nitrate ($NO_{3,Org}$) to the measured nitrate based on the ratio of NO_2^+ and NO^+ (Farmer et al., 2010; Fry et al., 2018; Kiendler-Scharr et al., 2016; Reyes-Villegas et al., 2018; Xu et al., 2015). Concentrations of $NO_{3,Org}$ were calculated following the method described by Farmer et al., 2010:

$$x_{NO_{3,Org}} = \frac{(R_{obs}-R_{cal})\,(1+R_{ON})}{(R_{ON}-R_{cal})\,(1+R_{obs})}\,, \tag{S5}$$

where R_{obs} is the ratio between m/z 46 and m/z 30 (NO_2^+/NO^+) observed over the dataset; R_{cal} is the ratio during ammonium nitrate calibrations; and R_{ON} is the ratio for organic nitrates. $R_{cal} = 0.56$ is the average of all ammonium nitrate calibrations reported in table S3 (ratios between 0.56 and 0.57 during all the calibrations). Following Kiendler-Scharr et al. (2016) and Kostenidou et al. (2015), the minimum ratio NO_2^+/NO^+ observed for the dataset (0.1 , Figure S) was selected for R_{ON} . R_{ON}, R_{cal} and R_{ON}/R_{cal} values obtained were consistent with previously reported values (Boyd et al., 2015; Bruns et al., 2010; Farmer et al., 2010; Kiendler-Scharr et al., 2016). Finally, $NO_{3,Org}$ concentrations in µg.m^{-3} were calculated as below:

$$NO_{3,Org} = x_{NO_{3,Org}}.NO_3^-\,, \tag{S6}$$

where NO_3^- is the total nitrate measured by the ToF-ACSM. We assume there is no interference from CH_2O^+ at m/z 30 and $CH_2O_2^+$ at m/z 46 as mentioned in section 2.2.1. This expression only applies if NH_4NO_3 is the major inorganic nitrate addition to organic nitrate in submicron particles. Some inorganics salts of nitrate such as $NaNO_3$ can give very small NO_2^+/NO^+ ratio especially for coastal site like Marseille, and could contribute to the observed NO_2^+/NO^+ ratio. Only concentrations of Na^+ were available with daily PM_1 filters measurements in 2017 and their different behaviour from $NO_{3,Org}$ daily concentrations let suppose that no interference comes from Na^+ (Figure S).

The average $NO_{3,Org}$ fraction for the whole dataset was 20±7%. The error is determined from error propagation calculations described by Farmer et al. (2010) derived from the different ratios (R_{obs}, R_{cal}, R_{ON}) uncertainties. The standard error of the mean was used as uncertainty associated with R_{obs} and R_{cal} and an estimated uncertainty of ±20% was used for R_{ON}.

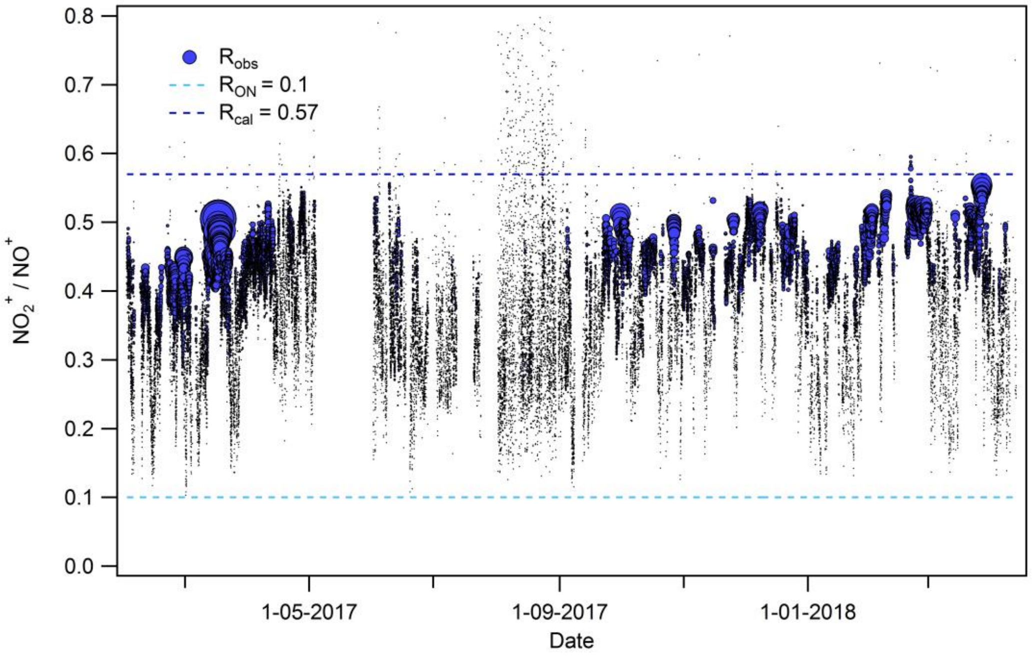

Figure S9. NO_2^+/NO^+ ratio over the measurement period. Marker sizes are proportional to the NO_3^- concentrations. R_{ON} dashed line is the ratio estimated for organic nitrates (minimum NO_2^+/NO^+ ratio observed on the dataset) and R_{cal} dashed line represents the averaged ratio during ammonium nitrate calibrations.

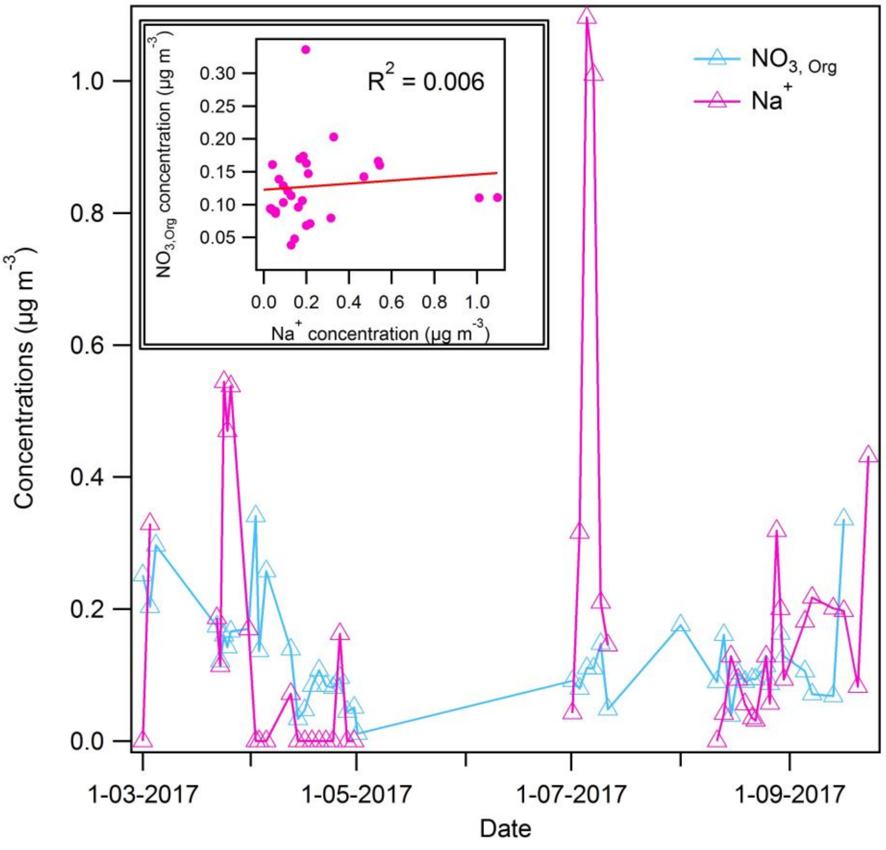

Figure S10. Comparison of $NO_{3,Org}$ calculated from ACSM data and Na^+ concentrations from PM_1 filters. Salts of nitrate such as $NaNO_3$ can be interfering inorganic species, with low NO_2^+/NO^+ ratio as for organic nitrates. Here there is no correlation between Na^+ and calculated $NO_{3,Org}$ variations over time.

Spring		Summer		Autumn		Winter	
lower	upper	lower	upper	lower	upper	lower	upper
0.18	0.28	0.06	0.10	0.11	0.17	0.14	0.2

Table S4. Overview of ON/OA ratio (nitrated organics vs organic aerosol) for all seasons. Lower and upper bounds correspond to an assumed molecular weight for particle-phase organic nitrate of 200 and 300 g mol^{-1}, respectively.

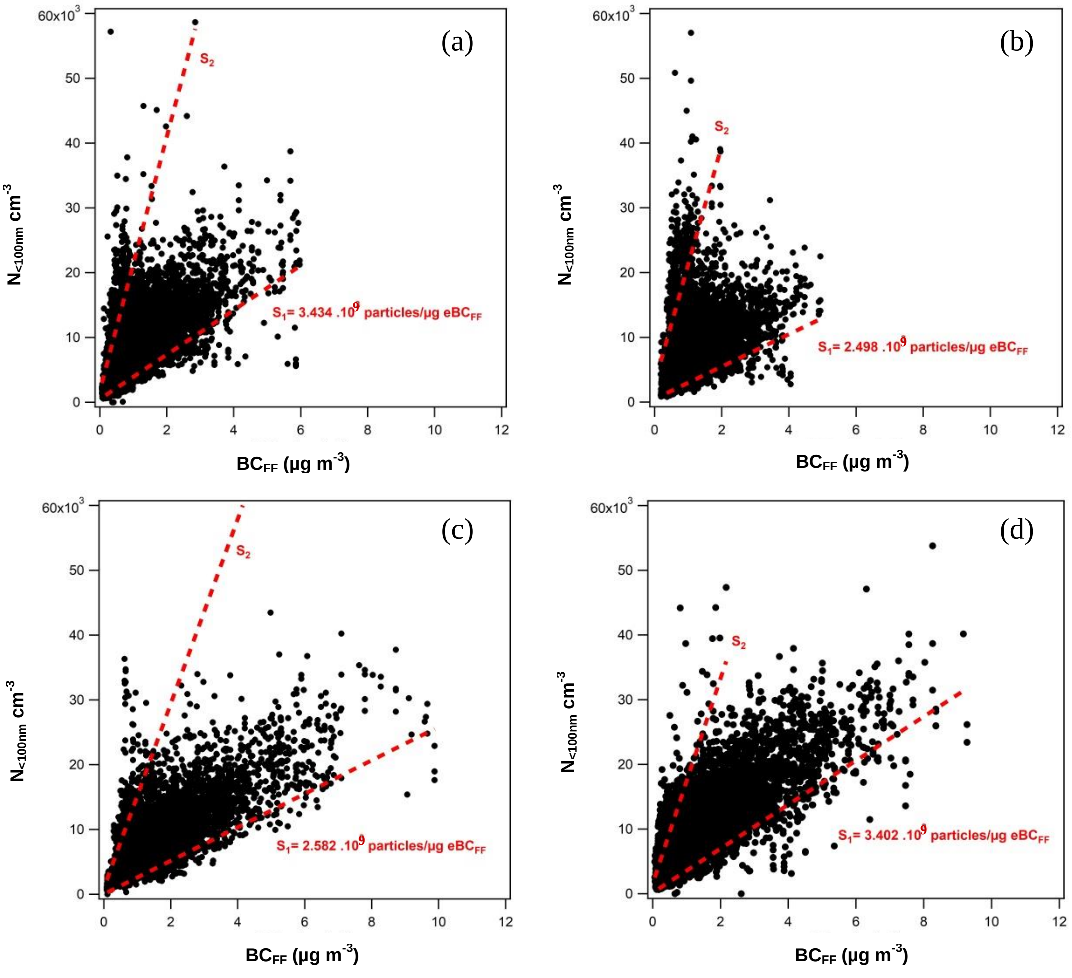

Figure S11. N (20 to 100 nm) from 3031 ultrafine particle monitor measurements vs BC$_{FF}$ scatter plot for spring (a), summer (b), autumn (c) and winter (d). BC data were smoothed with 1h-median to avoid spikes which can skew the linear regressions. S1 and S2 indicate the lines of the minimum and maximum slopes, respectively. S$_1$ is estimated using best-fit line to the points aligned in the lower edge of N vs BC$_{FF}$ scatter plot. The lower edge is defined according to all data below the 10th percentile of N/BC$_{FF}$.

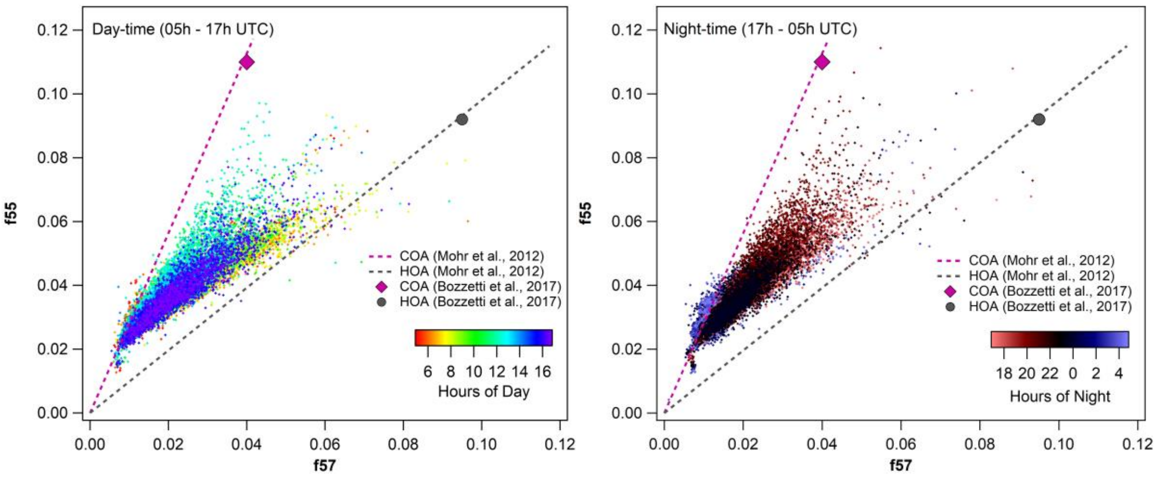

Figure S12. f55 vs f57 plots based on Mohr et al. (2012) over the study period. Day-time points (05h to 17h UTC) are displayed on the left graph and night-time data points (17h to 05h UTC) on the right graph. Data points are color-coded according to the hours of a day. Dashed lines represent the fits applied to hydrocarbon-like organic aerosol (HOA) and cooking organic aerosol (COA) data from Mohr et al. (2012) and pink diamonds and grey circles indicate f55 vs f57 of COA and HOA, respectively, from Bozzetti et al. (2017) study.

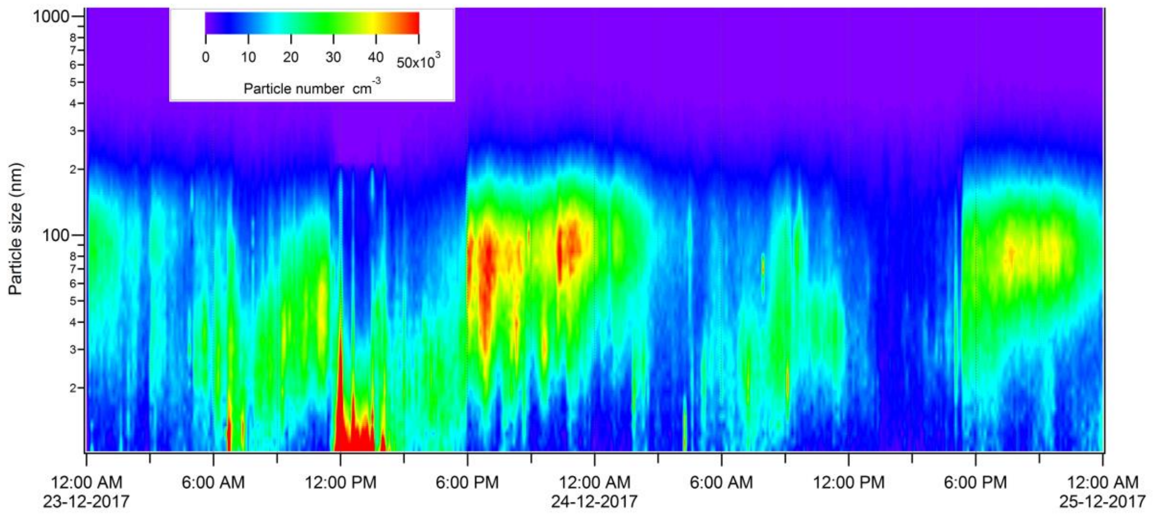

Figure S13. Particle number size distribution (dN/dlogdP) measured by the SMPS during the Christmas event (23-24 December 2017).

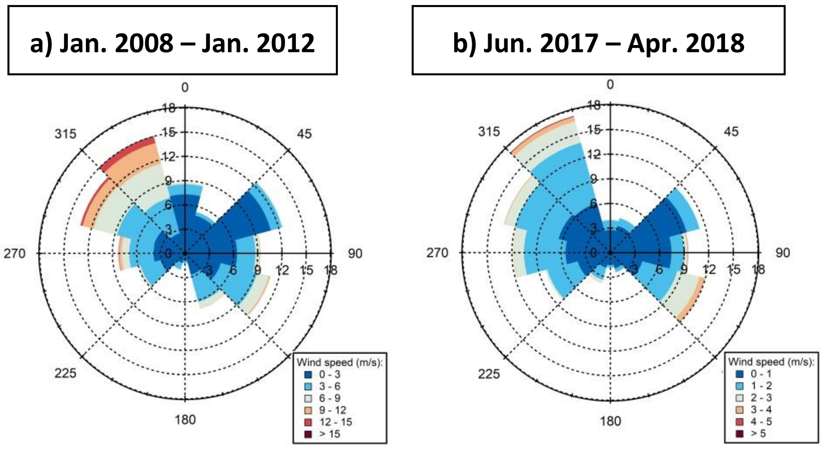

Figure S14. Wind roses for the hippodrome station (a) from January 2008 to January 2012 and MRS-LCP station (b) from June 2017 to April 2018. Tangential axe provide the wind direction (°) and radial axe the wind frequency (%). Wind direction clusters are color-coded according to the wind intensity (m.s^{-1}). This figure highlights that, despite the similar winds directions recorded at the two locations, wind speeds are at a lower level for MRS-LCP. This might be linked to the station surrounding area (i.e. large trees in the Longchamp park) reducing the actual wind speeds.

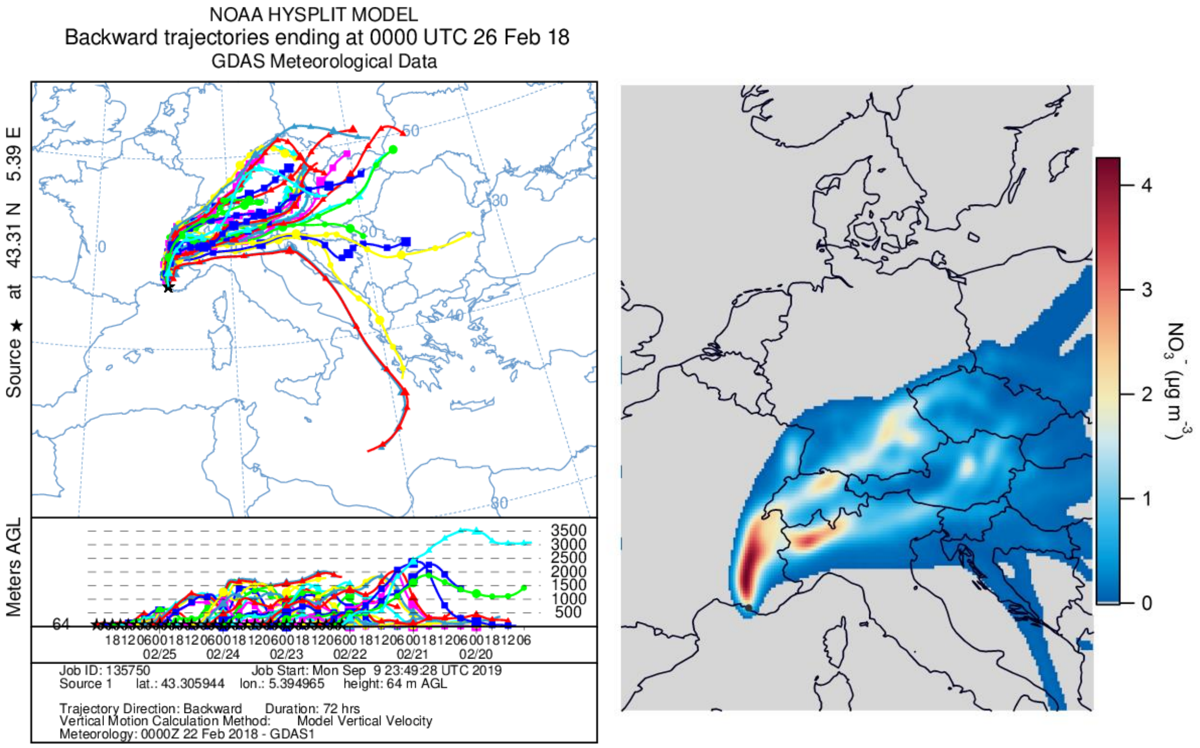

Figure S15. HYSPLIT air mass 72h-backtrajectories (left) and CWT maps for NO_3^- in µg m^{-3} (right) during the long-range episodes of February 2018 at MRS-LCP. The lower part of HYSPLIT panel show the air mass altitudes (in meters AGL) over the time.

Polluted days	**$PM_{2.5}$ (µg m^{-3})**	**BC/SO_4^{2-}**	**f44/f60**	**fNO_3^- $_{PM1}$ (%)**	**$fBC_{WB\ PM2.5}$ (%)**	**$fBC_{FF\ PM2.5}$ (%)**	**WS (m s^{-1})**	**$\Delta PM_{2.5}$ (Land breeze/Other winds) (%)**
14/03/2017	**26.0**	**0.9**	**18.3**	**29.0**	**1.7**	**6.1**	**1.8**	**-3.9**
15/03/2017	**30.0**	**1.4**	**16.7**	**23.3**	**2.3**	**7.7**	**1.7**	**-9.8**
16/03/2017	**28.0**	**1.2**	**22.0**	**23.6**	**1.9**	**7.5**	**2.0**	36.6
17/03/2017	**32.6**	**0.7**	**24.0**	**29.1**	**1.1**	**6.1**	**2.0**	**-11.9**
17/11/2017	**30.2**	**-**	-	**-**	**7.7**	**18.0**	**0.5**	**36.8**
05/12/2017	**28.0**	**12.7**	13.3	**7.5**	**7.8**	**14.0**	**0.7**	**68.7**
23/12/2017	**30.7**	**7.0**	**6.9**	**6.0**	**10.3**	**12.6**	**0.6**	**94.4**
24/12/2017	**31.8**	**5.3**	**6.4**	**11.0**	**8.3**	**8.0**	**0.7**	**70.3**
09/02/2018	**30.4**	**-**	-	**-**	**3.8**	**8.0**	**0.7**	**32.5**
16/02/2018	**29.0**	**-**	-	**-**	**4.2**	**13.0**	**0.6**	**12.1**
22/02/2018	**36.0**	**1.1**	10.0	**25.9**	**3.6**	**6.1**	0.8	**-1.6**
23/02/2018	**41.4**	**1.0**	**14.3**	**26.5**	**2.9**	**6.3**	0.8	11.3
24/02/2018	**37.5**	**1.3**	**11.3**	**23.0**	**3.1**	**7.7**	0.5	**-1.2**
25/02/2018	**31.9**	**1.0**	**12.5**	**24.6**	**3.1**	**6.2**	0.8	**0.9**
27/02/2018	**25.3**	**1.0**	**12.5**	**23.5**	**3.5**	**5.1**	**1.1**	16.6

Table S5. List of criteria used for the classification of polluted days. In addition to the $PM_{2.5}$ concentrations exceeding the WHO recommendation, other features were inspected: BC/SO_4^{2-}, f44/f60, the fraction of NO_3^- in PM_1, the fraction of BC_{WB} in $PM_{2.5}$, the fraction of BC_{FF} in $PM_{2.5}$, the wind speed and the difference between $PM_{2.5}$ concentrations associated with land breeze and with other wind sectors. Bold numbers indicate the fulfilled criteria. From the list, blue days are categorized as long-range events and red days as local events. Due to instrumental issues ACSM data were not available during the 17/11/2017, 09/02/2018 and 16/02/2018.

K-means clustering analysis applied to diurnal sulfate concentrations in summer:

Similarly to the Angström exponent's selection (see "The Angström exponent's determination" section in the Supplement) k-means clustering analysis was performed to categorize the several origins of sulfate concentrations in summer. The input matrix used consisted of hourly sulfate concentrations recorded for all days in summer (from 1 June to 31 August 2017). Days with more than 15% of missing values were excluded from the analysis, whereas the missing points from the remaining days were smoothed with median values. Since the k-means clustering algorithm includes distance-based measurements to determine the similarities between data points, sulfate data were normalized as the concentrations in the dataset show a large range of values (from 0 to 10.5 µg m^{-3}). A mean normalization was achieved:

$$x_{norm} = \frac{x - \bar{x}}{\max(x) - \min(x)} \qquad \text{(S7)}$$

With $\bar{x}$ the mean concentration for each day and $\max(x)$ and $\min(x)$ are the maximum/minimum values. Regarding the selection of the right number of clusters, the minimum value in the cost function is explored in the same way as Angström exponent's selection. Based on Figure S16 a minimum value is found for 6 clusters.

However, this number induces a too fragmented partitioning of data as some clusters patterns are not well explained. Thus the elbow method is applied to determine the optimal number of cluster (*k*). Based on this method, the spot where T1 stops dropping quickly with increasing *k*, and starts to flatten out and forming an elbow should correspond to the good number of cluster. According to Figure S16, the 3 and 4 clusters solutions seem appropriated choices. In the end 3 clusters were used as the solution was environmentally meaningful. Data points from all days and the 3 assigned clusters' centroids are represented in Figure S17.

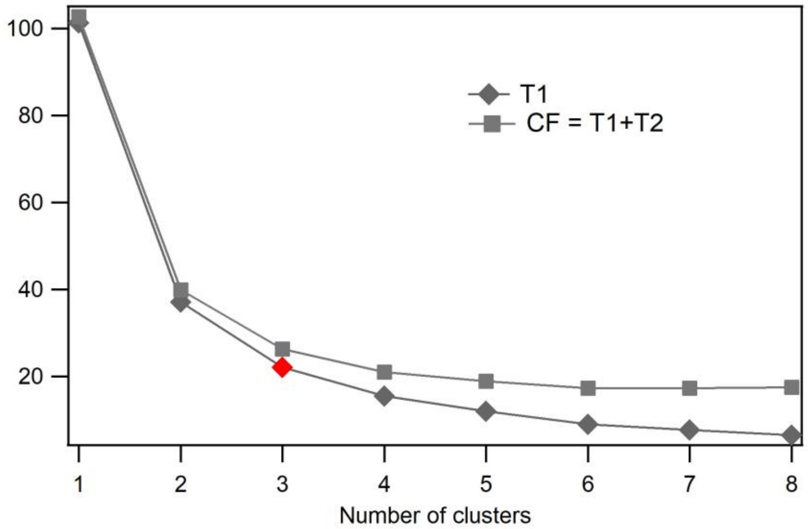

Figure S16. Number of cluster selection according to T1 (diamond markers) and the cost function (T1+T2) (square markers). The red marker represents the optimal number of cluster selected according to the elbow method.

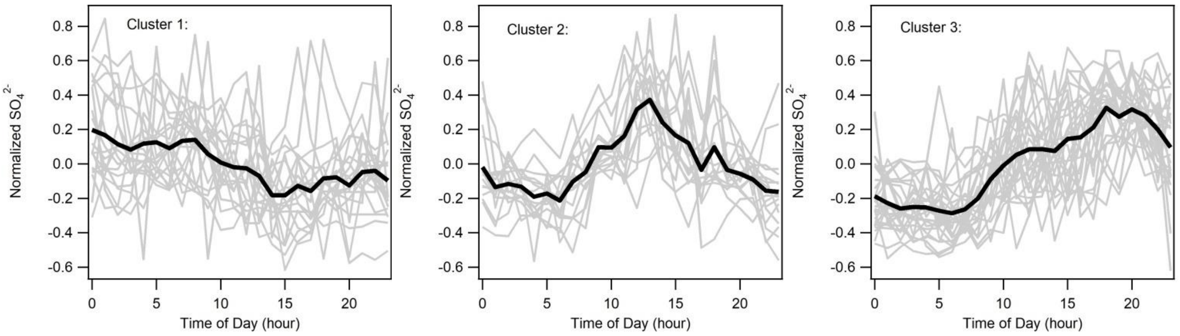

Figure S17. Results from the cluster analysis of the normalized SO_4^{2-} diurnal cycles in summer 2017. Three clusters are presented. Black lines are the clusters' centroids and grey lines represent normalized SO_4^{2-} hourly concentrations from each day.

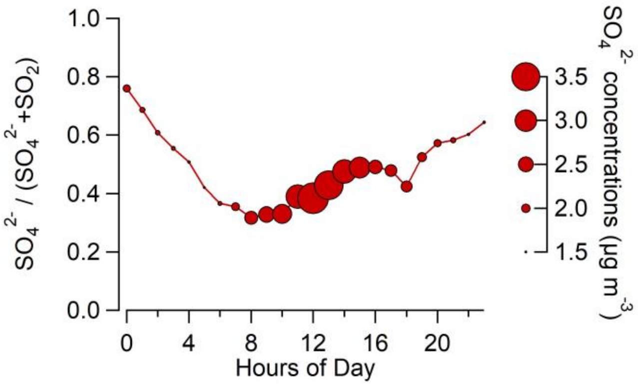

Figure S18. Daily cycle of SO_4^{2-} to total sulfur (SO_4^{2-}+SO_2) molar ratio observed for cluster 2.

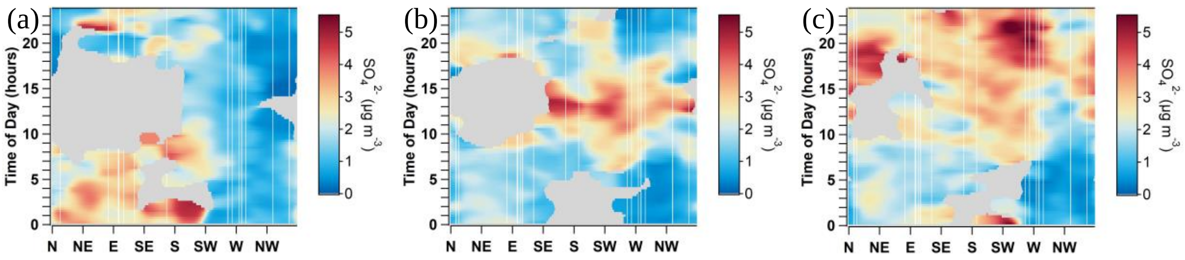

Figure S19. NWR plots representing the SO_4^{2-} concentrations as a function of hours of the day and wind direction in Cartesian coordinates. These representations are provided for cluster 1 (a), cluster 2 (b) and cluster 3 (c).

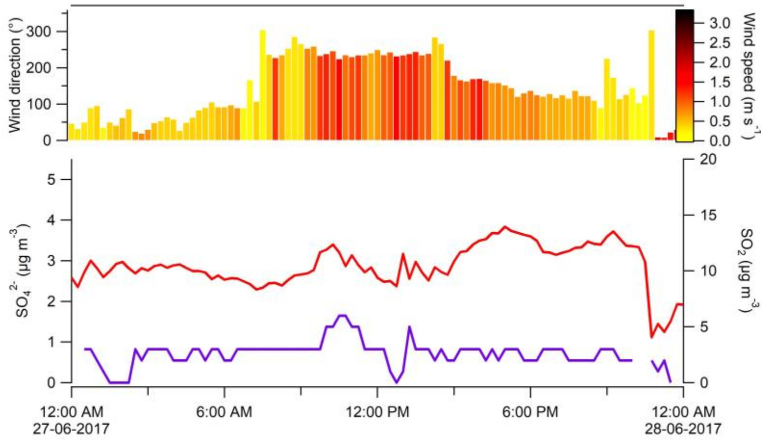

Figure S20. Time series of SO_4^{2-}, SO_2 and wind direction during 28 June, which is included in cluster 3. The wind direction is color-coded according to the wind speed.

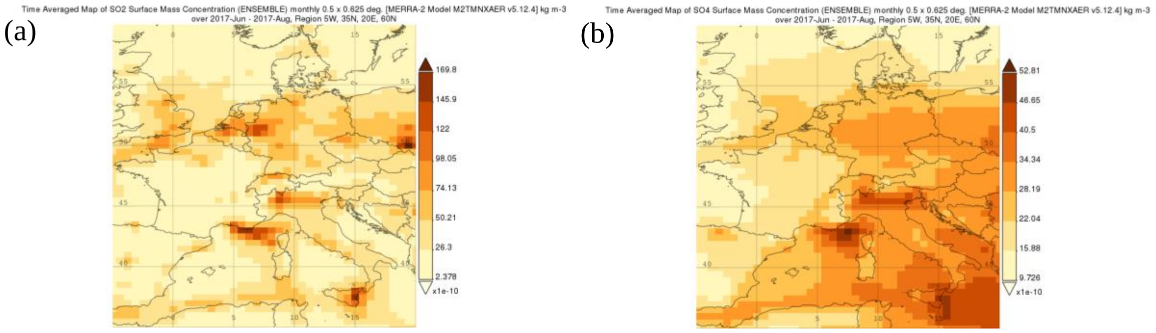

Figure S21. Summer 2017 average of SO_2 (a) and SO_4^{2-} (b) surface mass concentrations (in kg m^{-3}) calculated from the MERRA2 model (region: 5W-20E, 35N-60N). Maps are provided using GIOVANNI (GES-DISC Interactive Online Visualization And aNalysis Infrastructure) (Acker and Leptoukh, 2007).

			Cluster 1	Cluster 2	Cluster 3
			n=1920	n=1536	n=2592
OA	Average	µg m^{-3}	3.85	5.15	4.7
	SD	µg m^{-3}	2.47	3.02	2.45
BC	Average	µg m^{-3}	1.08	1.78	1.5
	SD	µg m^{-3}	0.73	1.55	1.01
SO_4^{2-}	Average	µg m^{-3}	1.86	2.25	2.56
	SD	µg m^{-3}	1.59	1.52	1.67
$NH4^+$	Average	µg m^{-3}	0.78	0.91	0.95
	SD	µg m^{-3}	0.56	0.53	0.55
$NO3^-$	Average	µg m^{-3}	0.22	0.25	0.25
	SD	µg m^{-3}	0.23	0.2	0.24
Cl^-	Average	µg m^{-3}	0.04	0.04	0.04
	SD	µg m^{-3}	0.02	0.13	0.02

Table S6. Averaged concentrations and associated standard deviation (SD) of chemical species from submicron aerosol for the three clusters. The "n" corresponds to the number of 15-min data points included in each cluster.

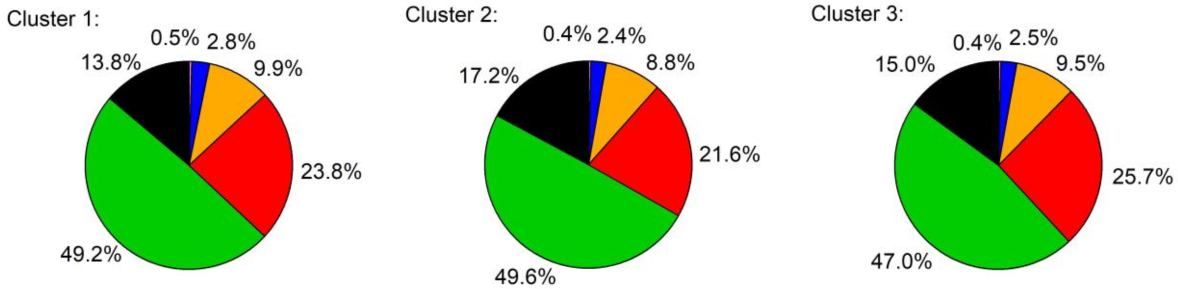

Figure S22. Chemical species contributions to PM_1 for the three clusters.

Supporting references

Acker, J. G. and Leptoukh, G.: Online Analysis Enhances Use of NASA Earth Science Data, Eos Trans. Am. Geophys. Union, 88(2), 14, https://doi.org/10.1029/2007EO020003, 2007.

Boyd, C. M., Sanchez, J., Xu, L., Eugene, A. J., Nah, T., Tuet, W. Y., Guzman, M. I. and Ng, N. L.: Secondary organic aerosol formation from the β-pinene+NO3 system: effect of humidity and peroxy radical fate, Atmospheric Chem. Phys., 15(13), 7497–7522, https://doi.org/10.5194/acp-15-7497-2015, 2015.

Bozzetti, C., El Haddad, I., Salameh, D., Daellenbach, K. R., Fermo, P., Gonzalez, R., Minguillón, M. C., Iinuma, Y., Poulain, L., Elser, M., Müller, E., Slowik, J. G., Jaffrezo, J.-L., Baltensperger, U., Marchand, N. and Prévôt, A. S. H.: Organic aerosol source apportionment by offline-AMS over a full year in Marseille, Atmospheric Chem. Phys., 17(13), 8247–8268, https://doi.org/10.5194/acp-17-8247-2017, 2017.

Bruns, E. A., Perraud, V., Zelenyuk, A., Ezell, M. J., Johnson, S. N., Yu, Y., Imre, D., Finlayson-Pitts, B. J. and Alexander, M. L.: Comparison of FTIR and Particle Mass Spectrometry for the Measurement of Particulate Organic Nitrates, Environ. Sci. Technol., 44(3), 1056–1061, https://doi.org/10.1021/es9029864, 2010.

Elser, M., Huang, R.-J., Wolf, R., Slowik, J. G., Wang, Q., Canonaco, F., Li, G., Bozzetti, C., Daellenbach, K. R., Huang, Y., Zhang, R., Li, Z., Cao, J., Baltensperger, U., El-Haddad, I. and Prévôt, A. S. H.: New insights into PM2.5 chemical composition and sources in two major cities in China during extreme haze events using aerosol mass spectrometry, Atmospheric Chem. Phys., 16(5), 3207–3225, https://doi.org/10.5194/acp-16-3207-2016, 2016.

Farmer, D. K., Matsunaga, A., Docherty, K. S., Surratt, J. D., Seinfeld, J. H., Ziemann, P. J. and Jimenez, J. L.: Response of an aerosol mass spectrometer to organonitrates and organosulfates and implications for atmospheric chemistry, Proc. Natl. Acad. Sci., 107(15), 6670–6675, https://doi.org/10.1073/pnas.0912340107, 2010.

Fry, J. L., Brown, S. S., Middlebrook, A. M., Edwards, P. M., Campuzano-Jost, P., Day, D. A., Jimenez, J. L., Allen, H. M., Ryerson, T. B., Pollack, I., Graus, M., Warneke, C., de Gouw, J. A., Brock, C. A., Gilman, J., Lerner, B. M., Dubé, W. P., Liao, J. and Welti, A.: Secondary organic aerosol (SOA) yields from NO<sub>3</sub> radical + isoprene based on nighttime aircraft power plant plume transects, Atmospheric Chem. Phys., 18(16), 11663–11682, https://doi.org/10.5194/acp-18-11663-2018, 2018.

Garg, S., Chandra, B. P., Sinha, V., Sarda-Esteve, R., Gros, V. and Sinha, B.: Limitation of the Use of the Absorption Angstrom Exponent for Source Apportionment of Equivalent Black Carbon: a Case Study from the North West Indo-Gangetic Plain, Environ. Sci. Technol., 50(2), 814–824, https://doi.org/10.1021/acs.est.5b03868, 2016.

Kiendler-Scharr, A., Mensah, A. A., Friese, E., Topping, D., Nemitz, E., Prevot, A. S. H., Äijälä, M., Allan, J., Canonaco, F., Canagaratna, M., Carbone, S., Crippa, M., Dall Osto, M., Day, D. A., De Carlo, P., Di Marco, C. F., Elbern, H., Eriksson, A., Freney, E., Hao, L., Herrmann, H., Hildebrandt, L., Hillamo, R., Jimenez, J. L., Laaksonen, A., McFiggans, G., Mohr, C., O'Dowd, C., Otjes, R., Ovadnevaite, J., Pandis, S. N., Poulain, L., Schlag, P., Sellegri, K., Swietlicki, E., Tiitta, P., Vermeulen, A., Wahner, A., Worsnop, D. and Wu, H.-C.: Ubiquity of organic nitrates from nighttime chemistry in the European submicron aerosol: Organic Nitrates in European PM1, Geophys. Res. Lett., 43(14), 7735–7744, https://doi.org/10.1002/2016GL069239, 2016.

Kostenidou, E., Florou, K., Kaltsonoudis, C., Tsiflikiotou, M., Vratolis, S., Eleftheriadis, K. and Pandis, S. N.: Sources and chemical characterization of organic aerosol during the summer in the eastern Mediterranean, Atmospheric Chem. Phys., 15(19), 11355–11371, https://doi.org/10.5194/acp-15-11355-2015, 2015.

Mohr, C., DeCarlo, P. F., Heringa, M. F., Chirico, R., Slowik, J. G., Richter, R., Reche, C., Alastuey, A., Querol, X., Seco, R., Peñuelas, J., Jiménez, J. L., Crippa, M., Zimmermann, R., Baltensperger, U. and Prévôt, A. S. H.: Identification and quantification of organic aerosol from cooking and other sources in Barcelona using aerosol mass spectrometer data, Atmospheric Chem. Phys., 12(4), 1649–1665, https://doi.org/10.5194/acp-12-1649-2012, 2012.

Petit, J.-E., Amodeo, T., Meleux, F., Bessagnet, B., Menut, L., Grenier, D., Pellan, Y., Ockler, A., Rocq, B., Gros, V., Sciare, J. and Favez, O.: Characterising an intense PM pollution episode in March 2015 in France from multi-site approach and near real time data: Climatology, variabilities, geographical origins and model evaluation, Atmos. Environ., 155, 68–84, https://doi.org/10.1016/j.atmosenv.2017.02.012, 2017.

Reyes-Villegas, E., Priestley, M., Ting, Y.-C., Haslett, S., Bannan, T., Le Breton, M., Williams, P. I., Bacak, A., Flynn, M. J., Coe, H., Percival, C. and Allan, J. D.: Simultaneous aerosol mass spectrometry and chemical ionisation mass spectrometry measurements during a biomass burning event in the UK: insights into nitrate chemistry, Atmospheric Chem. Phys., 18(6), 4093–4111, https://doi.org/10.5194/acp-18-4093-2018, 2018.

Titos, G., del Águila, A., Cazorla, A., Lyamani, H., Casquero-Vera, J. A., Colombi, C., Cuccia, E., Gianelle, V., Močnik, G., Alastuey, A., Olmo, F. J. and Alados-Arboledas, L.: Spatial and temporal variability of carbonaceous aerosols: Assessing the impact of biomass burning in the urban environment, Sci. Total Environ., 578, 613–625, https://doi.org/10.1016/j.scitotenv.2016.11.007, 2017.

Xu, L., Suresh, S., Guo, H., Weber, R. J. and Ng, N. L.: Aerosol characterization over the southeastern United States using high-resolution aerosol mass spectrometry: spatial and seasonal variation of aerosol composition and sources with a focus on organic nitrates, Atmospheric Chem. Phys., 15(13), 7307–7336, https://doi.org/10.5194/acp-15-7307-2015, 2015.

Zotter, P., Herich, H., Gysel, M., El-Haddad, I., Zhang, Y., Močnik, G., Hüglin, C., Baltensperger, U., Szidat, S. and Prévôt, A. S. H.: Evaluation of the absorption Ångström exponents for traffic and wood burning in the Aethalometer-based source apportionment using radiocarbon measurements of ambient aerosol, Atmospheric Chem. Phys., 17(6), 4229–4249, https://doi.org/10.5194/acp-17-4229-2017, 2017.